Title

Nanoporous-Gold-Based Electrode Morphology Libraries for Investigating Structure–Property Relationships in Nucleic Acid Based Electrochemical Biosensors

Journal

ACS Applied Materials & Interfaces, 9(15)

ISSN

1944-8244

Authors

Matharu, Zimple
Daggumati, Pallavi
Wang, Ling
et al.

Publication Date

2017-04-19

DOI

10.1021/acsami.6b15212

ACS APPLIED MATERIALS & INTERFACES

Article

Nanoporous Gold-Based Electrode Morphology Libraries for Investigating Structure-Property Relationships in Nucleic Acid-Based Electrochemical Biosensors

Zimple Matharu, Pallavi Daggumati, Ling Wang, Tatiana S. Dorofeeva, Zidong Li, and Erkin Seker

ACS Appl. Mater. Interfaces, **Just Accepted Manuscript** • Publication Date (Web): 17 Jan 2017

Just Accepted

ACS Publications

ACS Applied Materials & Interfaces is published by the American Chemical Society.
1155 Sixteenth Street N.W., Washington, DC 20036

Nanoporous Gold-Based Electrode Morphology Libraries for Investigating Structure-Property Relationships in Nucleic Acid-Based Electrochemical Biosensors

Zimple Matharu[1], Pallavi Daggumati[1], Ling Wang[1], Tatiana S. Dorofeeva[1], Zidong Li[2], Erkin Seker[1,*]

[1]Departments of Electrical and Computer Engineering and [2]Biomedical Engineering

University of California - Davis, Davis, California 95616, United States

Correspondence: eseker@ucdavis.edu

ABSTRACT

Nanoporous gold (np-Au) electrode coatings significantly enhance the performance of electrochemical nucleic acid biosensors due to their three-dimensional nanoscale network, high electrical conductivity, facile surface functionalization, and biocompatibility. Contrary to planar electrodes, the np-Au electrodes also exhibit sensitive detection in the presence of common biofouling media due to their porous structure. However, the pore size of the nano-matrix plays a critical role in dictating the extent of biomolecular capture and transport. Small pores perform better in case of target detection in complex samples by filtering out the large non-specific proteins. On the other hand, larger pores increase the accessibility of target nucleic acids into the nanoporous structure, enhancing detection limits of the sensor yet at the expense of more interference from biofouling molecules. Here, we report a microfabricated np-Au multiple electrode array that displays a range of electrode morphologies on the same chip for identifying feature sizes that reduce the non-specific adsorption of proteins but facilitate the permeation of target DNA molecules into the pores. We demonstrate the utility of the electrode morphology library (EML) in studying DNA functionalization and target detection in complex biological media with a special emphasis on revealing ranges of electrode morphologies that mutually enhance limit of detection and biofouling resilience. We expect this technique to assist in the development of high-performance biosensors for point-of-care diagnostics and facilitate studies on electrode structure-property relationships in potential applications ranging from neural electrodes to catalysts.

KEYWORDS: Nanoporous gold, electrochemical coarsening, nucleic acid-based biosensors, high-throughput material screening, biofouling, multiple electrode array.

1. INTRODUCTION

Electrochemical biosensors have proven to be promising bioanalytical tools for nucleic acid detection[1,2]. One of the major advantages of these sensors over other detection modalities (e.g., optical, magnetic, and mechanical) is their multiplexing capabilities through seamless integration with signal processing electronics. Despite these advantages, electrochemical sensing platforms have suffered from low sensitivity and limit of detection due to electrode fouling in complex biological media[3-4]. Since the sensing electrode is a vital component of electrochemical biosensors, the advent of nanostructured electrodes benefited sensitivity and detection limits of these biosensors by providing high surface area-to-volume ratio[5,6-7-8] and unique features such as biofouling resilience while operating in complex biological samples (e.g., serum, cell lysate, whole blood)[9, 10]. One such emerging nanostructured material, nanoporous gold (np-Au) fabricated by a corrosion-driven self-assembly process, has demonstrated significant promise due to its tunable morphology, high electrical conductivity, chemical/mechanical stability, facile functionalization with thiol-gold chemistry, and high surface-to-volume ratio[11-12-13]. For np-Au and other nanostructured electrodes, the extent of nanostructure dictates the performance parameters of electrochemical biosensor. A major challenge is that nanostructure influences sensor performance parameters non-uniformly, that is, while characteristic nanostructure size may be directly proportional to limit of detection, it may be inversely proportional to biofouling resilience[14]. This highlights the need for a capability to test multiple nanostructures in parallel. While microfabrication technology allows for creating multiple electrode arrays (MEAs), it is not trivial to produce an MEA where the nanostructure of each electrode is independently and precisely controlled.

There has been significant research on strategies to control the morphology of np-Au electrodes, particularly dealloyed white-gold foils and ingots cut into various shapes[11, 15]. The most common among morphology modification is coarsening of the ligaments and the pores either by thermal annealing or by treatment with concentrated acid for prolonged periods[16-17]. However, since these techniques expose the entire MEA, they are not conducive to generating a library of diverse nanostructures on a single chip. To that end, electrochemical cycling of gold thin films in presence of anions, which is known to enhance the surface roughness, is a promising method to

address this issue[18-20]. During this process, the rearrangement of gold atoms occur due to their enhanced surface diffusion in the presence of anions[21]. The level of surface atom diffusivity, consequently the degree of coarsening, depends on the electrolyte, as well as the extent and strength of the surface adsorption of anions, which is a function of the applied electrochemical potential[20, 22]. The goal of this paper is to employ micropatterning techniques and in situ room-temperature electrochemical coarsening method to create a np-Au MEA that displays a range of pore morphologies on a single chip, which we refer to as *electrode morphology library* (EML). We initially report results on the influence of pore morphology on mass transport of redox reporters in np-Au electrodes, which plays an essential role in sensor performance. We then demonstrate the utility of the EML in studying DNA functionalization and target detection in complex biological media with a special emphasis on revealing ranges of electrode morphologies that break even at several enhanced sensor performance parameters.

2. MATERIALS AND METHODS

2.1. Chemicals and Reagents

Glass coverslips (22 mm × 22 mm x 0.15 mm) from Electron Microscopy Sciences, USA were used as substrates for metal film deposition. Gold, silver, and chrome targets (99.95% pure) were purchased from Kurt J. Lesker. Methylene blue (MB), potassium ferricyanide [$K_3Fe(CN)_6$], potassium ferrocyanide [$K_4Fe(CN)_6$] and 6-(ferrocenyl)hexanethiol (Fc-SH) were purchased from Sigma-Aldrich, USA. Sulfuric acid (96%) and hydrogen peroxide (30%) were purchased from J. T. Baker. Glass cover slips were cleaned with Piranha solution as described earlier[23]. Tris(2-chloroethyl)phosphate (TCEP), magnesium chloride ($MgCl_2$), sodium phosphate monobasic, and sodium phosphate dibasic were obtained from Fisher Scientific. Phosphate bu□ered saline (PBS) and fetal bovine serum (FBS) was purchased from Life Technologies. The thiolated 26-mer probe DNA and its complimentary target were used to study the hybridization and the detailed DNA sequences are provided in our previous work [23].

2.2. Fabrication of np-Au Electrodes

The np-Au electrodes were fabricated using techniques that merges standard microfabrication techniques and Au-Ag alloy corrosion process, described previously[23]. For np-Au electrode fabrication, we used piranha-cleaned glass coverslips or standard microscope slides as substrates.

The electrodes consisted of a 160 nm-thick chrome adhesive layer, 80 nm-thick gold seed layer, and a 600 nm-thick gold-silver alloy (gold 36 At % and silver 64 At %)[23-24]. All layers were created by sputter deposition in argon at a pressure of 10 mTorr. In order to create the MEAs (8 electrodes of 1.25 mm-diameter, Scheme 1), the Ag-Au was patterned by laser ablation[25]. The non-patterned and laser patterned alloys were dealloyed in 70% nitric acid at 55°C for 15 min to obtain the np-Au structures having 5-8% residual silver, as measured by energy dispersive X-ray spectroscopy (EDS). Planar gold (pl-Au) electrodes were also fabricated by sputtering using previously described method[23]. For electrochemical measurements with non-patterned np-Au electrodes, a custom-built Teflon electrochemical cell was used to expose electrode footprint of 0.15 cm^2 as the working electrode. In order to integrate the np-Au MEA with the electrochemical setup, the traces connecting np-Au electrodes with the contact pads were insulated by a thin circular PDMS layer (inner diameter = 5.5 mm and outer diameter = 9.5 mm bonded via oxygen plasma). A glass cylinder was placed on top of the MEA to produce the electrochemical cell for coarsening and biosensing experiments (Scheme 1).

2.3. Microscopic Characterization of np-Au Electrodes

High-magnification images of the samples with di□erent morphologies were captured with a scanning electron microscope (SEM, FEI Nova NanoSEM430) to investigate micro- and nano-scale morphological features, as well as the thickness of np-Au films. The average pore sizes for different morphologies were analyzed using ImageJ software as described previously (National Institutes of Health shareware, http://rsb.info.nih.gov/ij/index.html)[23].

2.4. Electrochemical Measurements

The initial optimization of electrochemical coarsening and characterization of the np-Au morphologies via cyclic voltammetry (CV) was done in an Teflon electrochemical cell connected to Gamry Reference 600 potentiostat, while probe DNA immobilization and detection experiments were performed using the electrochemical cell integrated with np-Au MEA (Scheme 1). Both electrochemical setups utilized a platinum wire as counter electrode and a Ag/AgCl as reference electrode Square wave voltammetry (SWV) over the potential range of 0 to –0.6 V with a pulse amplitude of 40 mV, and pulse frequency of 60 Hz, was carried out to investigate DNA immobilization and target detection. The DNA experiments were performed separately in 1X PBS and in 10% fetal bovine serum (FBS), which served as complex media, to investigate

the influence of morphology on the sensor performance. Percentage suppression in MB signal (($I_{probe} - I_{target}$) / I_{probe}) x 100) was used as a measure of target DNA binding to the probe functionalized sensor surface.

2.5. Coarsening np-Au Electrodes via Cyclic Voltammetry (CV)

The np-Au working electrodes were coarsened at room temperature in the three electrode electrochemical setup described previously. Specifically, the coarsening was conducted by electrochemically-cycling the np-Au electrodes between 0.3 to 1.2 V in 100 mM H_2SO_4 with CV protocol. Different coarsening levels were achieved by changing the number of CV scans. The effective electrochemical surface area of each np-Au morphology was obtained by performing CV measurements in 0.5 M H_2SO_4 at a scan rate of 50 mV/s over the potential range 0 to 1.8 V [26].

2.6. Electrochemical Characterization of np-Au in Diffusion-Controlled and Surface-Confined Redox Molecules

Diffusion-controlled[27-28] and surface-confined markers[27-29] were used to determine the effect of morphology on redox and transport behavior of small redox molecules. For this we chose molecules having same redox moieties responsible for the electrochemical signal (i.e., potassium ferricyanide/ferrocynide $K_4[Fe(CN)_6]/K_3[Fe(CN)_6]$, and 6-(ferrocenyl)hexanethiol (Fc-SH) where $Fe^{2+/3+}$ is responsible for redox signaling). The Fc-SH self-assembles into a monolayer on np-Au via gold-thiol linkage, while potassium ferricyanide/ferrocynide remains in the solution. The electrochemical responses of both redox markers, were investigated at each np-Au electrode morphology. In the first set of experiments, np-Au morphologies were characterized in 5 mM $K_4[Fe(CN)_6]/K_3[Fe(CN)_6]$ solution in phosphate buffer (PB) via CV measurements. In another set of experiments, Fc-SH monolayers were prepared by immersing np-Au electrodes in an ethanoic solution of 5 mM Fc-SH for 12 h. These Fc-SH modified morphologically diverse np-Au electrodes were characterized in 0.1 M methansulfonic acid via CV at a scan rate of 50 mv/s.

2.7. Immobilization of Probe DNA on EML and Target DNA Detection

The disulfide bonds of probe DNA stock (100 μM) were reduced in 10 mM TCEP solution[23] for 1 h and excess TCEP was filtered out using spin columns . For electrode functionalization with the thiolated probe DNA molecules, the EML was incubated overnight at room temperature with

200 μL of 2 μM thiolated DNA probe solution prepared in 25 mM phosphate buffer (PB) comprising 50 mM $MgCl_2$. The unbound DNA molecules were removed by rinsing the electrodes with PB multiple times. The DNA modified electrodes were further incubated with 1 mM mercaptohexanol (MCH) for 1 h to block the unmodified sites and to obtain ordered mixed DNA-MCH monolayer.

To confirm successful DNA immobilization, the electrodes were incubated with 200 μL of 20 μM methylene blue (MB) prepared in 1X phosphate buffered saline (PBS) for 10 minutes [23]. The MB system has been routinely used by us [23] and others [30-34] previously to monitor DNA hybridization due to its differential interactions with single- and double-stranded DNA. The electrodes were rinsed after MB accumulation to remove unbound and non-specifically-bound molecules and square wave voltammetry (SWV) measurements were carried out in 1X PBS. For detection experiments, probe DNA-modified electrodes were incubated with 50 nM target DNA prepared either in PB containing 50 mM $MgCl_2$ (for non-complex media experiments) or 10% FBS (for complex media experiments) in PB comprising 50 mM $MgCl_2$ for 30 minutes at 37°C and MB accumulation step was performed again. The percentage signal suppression in the MB reduction current due to target binding was again determined using the formula, $(I_{probe} - I_{target}/I_{probe}) \times 100$. Scheme 1 outlines fabrication of the np-Au EML and its application to investigate the influence of np-Au morphology on electrochemical DNA sensor performance.

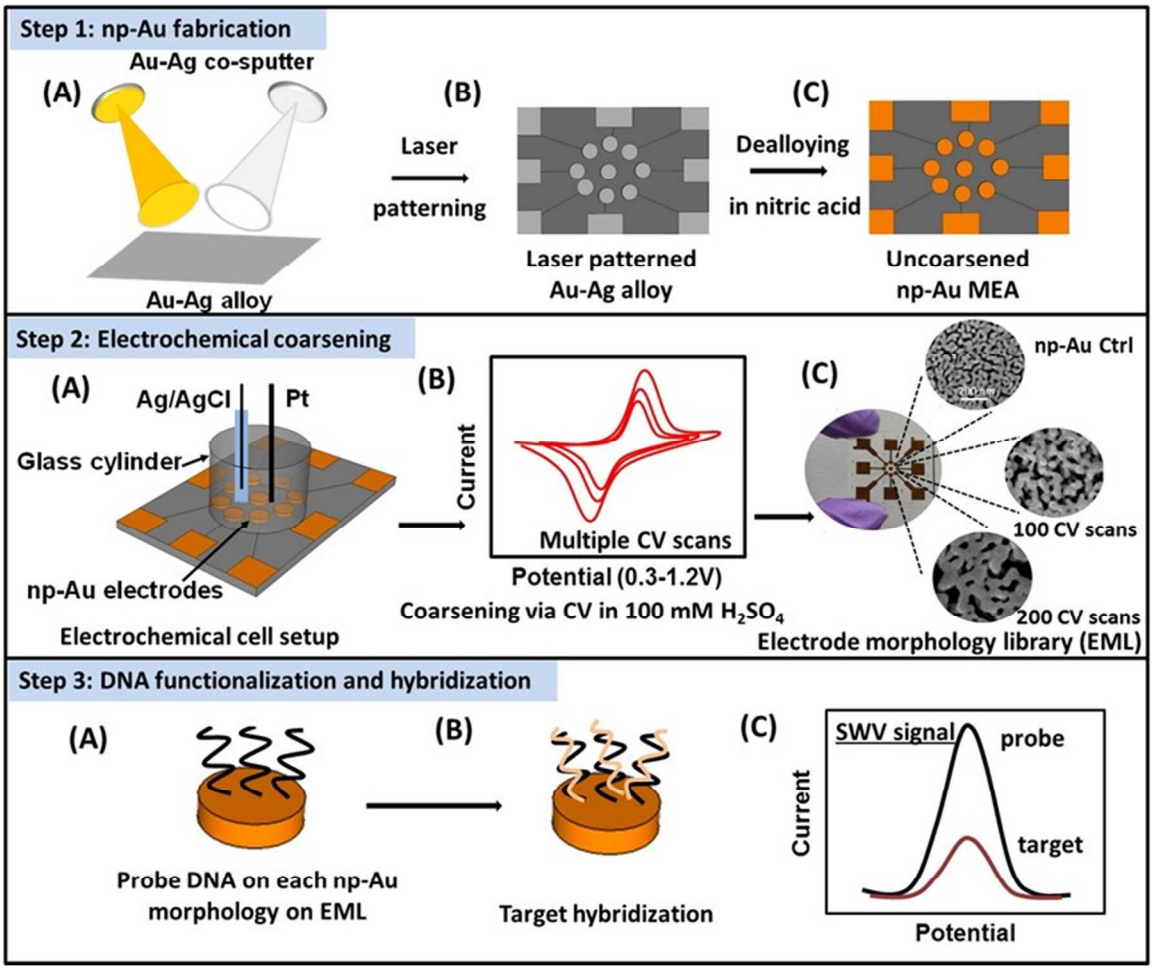

Scheme 1. Schematic illustration of a fabricated np-Au multiple electrode array (MEA) with an electrochemical cell for coarsening and biosensing studies. Step 1: (A) Co-sputtering Au-Ag alloy on glass and (B) creating the np-Au electrode array pattern via laser ablation followed by (C) dealloying in nitric acid to create np-Au electrodes. Step 2: (A) Integrating np-Au MEA into the electrochemical cell and (B) cycling each electrode in H_2SO_4 using cyclic voltammetry to (C) create EML having diverse coarser morphologies on a single chip. Step 3: (A) Functionalizing EML with thiolated probe DNA molecules and (B) investigating target hybridization via (C) square wave voltammetry.

3. RESULTS AND DISCUSSION

In order to address the inadequacies of existing annealing techniques (e.g., thermal annealing) that prevents coarsening of individual electrodes on a single chip, we leveraged potential-dependent surface diffusivity of gold atoms responsible for coarsening. This, combined with

facile integration of np-Au into microdevices, allowed for the fabrication of the electrode morphology library (EML) displaying a range of np-Au pore morphologies on a single chip (Scheme 1). This further allowed to investigate DNA immobilization and hybridization of different electrode morphologies.

3.1. Electrochemical Coarsening of np-Au Electrodes

In this section, we discuss the results of the room-temperature electrochemical method to create EML along with various parameters optimized to obtain different levels of np-Au coarsening while avoiding loss of gold via etching. The principle of electrochemical coarsening in the present study is based on multilayer gold oxide formation and reduction induced by electrochemical cycling of the gold electrodes in acid solutions[35]. The surface diffusion coefficient for gold atoms increases with applied voltage, consequently leading to a self-similar yet coarser morphology (Figure 1A) [19,36]. Electrochemical cycling of planar gold (pl-Au) in acid solutions has long been used for surface cleaning and investigating the surface area. However, this requires high concentrations of acid and a large potential window which can be harmful for multiple oxidation-reduction cycles on thin porous gold electrodes and may result in gold etching. In order to achieve coarsening of np-Au thin film electrodes, we first optimized the concentration of H_2SO_4 and the suitable electrochemical potential window. Specifically, standard np-Au electrodes were cycled between different voltages of 0.3-1.6 V, 0-1.2 V and 0.3-1.2 V in a custom-built Teflon electrochemical cell using np-Au as the working electrode, platinum wire as the counter electrode, and Ag/AgCl as the reference electrode. In these experiments, we observed that the application of potentials above 1.2 V resulted in gold etching as the ligaments appeared thinner (Figure S1, ii) and potentials below 0.3 V form large microstructures on top of the electrode surface (Figure S1, iii). The optimal np-Au coarsening was thus achieved in the potential range of 0.3 V-1.2 V (Figure 1A & Figure S1, iv), at which all subsequent electrochemical coarsening experiments were performed.

Figure 1A shows the SEM images of np-Au morphologies obtained after cycling the np-Au electrodes for 50, 100, 200, and 300 times over the potential range of 0.3 to 1.2 V (Figure 1B). The images demonstrate increased level of coarsening with increasing number of CV scans up to 200 cycles, while the thickness of np-Au remained unchanged (~410 nm, np-Au cross-section view shown in inset of Figure S1, iv). The images demonstrate that level of coarsening increases

with the increasing number of CV scans up to 200 cycles (Figure 1A, iv). Higher number of CV scans typically resulted in gold islands and gold etching in some regions of the electrode (Figure 1A, v). Pore radius (with circular pore approximation) extracted by analysis of the SEM images demonstrated the capability to produce a wide range of electrode morphologies (Figure 1C).

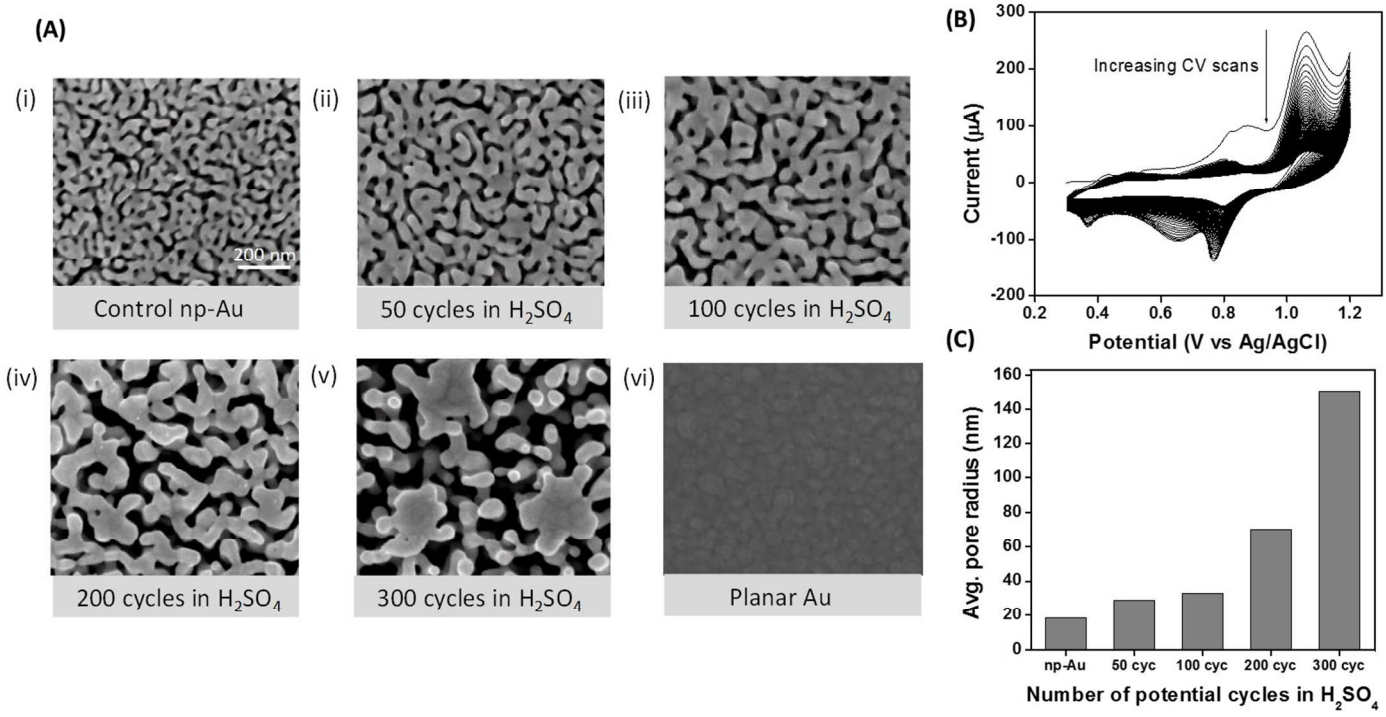

Figure 1. (A) (i)-(vi) SEM images of electrochemically-coarsened np-Au electrodes along with control planar Au electrode (vi). (B) Cyclic voltammograms depicting the coarsening process. (C) Average pore radius obtained by image analysis for a particular np-Au morphology.

3.2. Determination of Effective Surface Area

The effective surface area of the various nanoporous morphologies was determined by previously described protocols that discuss charge required to strip the gold oxide layer via CV (Supporting information, Figure S2). For this, we used higher concentration of sulfuric acid (0.5 M) [37-38] and conducted CV measurement over a potential window of 0 - 1.8 V [26]. The pl-Au and np-Au electrodes showed broad peaks in the range 1.2 to 1.4 V, plausibly due to the formation of gold oxide and a sharp reduction peak around 0.9 V (Figure S2). The electrical charge under the gold oxide reduction peak between the potentials 0.7 and 0.9 V was converted into the e□ective surface area by using 450 μC/cm^2 as the specific charge required for gold oxide reduction[39]

(Figure S2). The effective surface area decreased with increasing number of CV scans, that is, increased coarsening (inset of Figure S2).

3.3. Electrochemical Characterization of np-Au Morphologies in Surface-Confined and Diffusion-Controlled Redox Molecules

In order to effectively study the influence of electrode morphology on the biosensor performance, we first investigated how electrode morphology dictates the electrochemical signal from common redox markers. To that end, we chose 6-(ferrocenyl)hexanethiol (Fc-SH) and potassium ferrocyanide/ferricyanide ($K_4Fe(CN)_6/K_3Fe(CN)_6$) as model redox markers in the current studies (Supporting information, Figure S3 & S4). Both these redox markers contain 'Fe' as the redox center; however, the former serves as a surface-confined redox marker due to the thiol-functionalized ferrocenyl that creates a self-assembled monolayer on np-Au, while the latter is diffusion-controlled [27].

The behavior of both redox markers on different np-Au morphologies are shown in Figure S3 and Figure S4. The surface-bound iron atom led to oxidation and reduction peaks at 0.46 V and 0.40 V (Figure S3), while the di□usion-controlled redox marker $K_4Fe(CN)_6$/ $K_3Fe(CN)_6$ (Figure S4) produced redox peaks at 0.39 V and 0.05 V. We observed that the surface-confined redox marker was able to distinguish between different morphologies by showing 39%, 45%, and 56% change in the current values for morphologies with 50, 100 and 200 CV scans, respectively. Additionally, it displayed a 94% current change between uncoarsened np-Au and planar Au electrodes (Table S1). However, the diffusion-controlled marker showed only 13% current change for the coarser morphologies obtained by 50 CV scans and 41% current change for 200 CV scans. Also, the difference in current values was only 47% for uncoarsened np-Au and planar Au in $K_4Fe(CN)_6$/ $K_3Fe(CN)_6$ (Table S1). The current change values for both redox markers are summarized in Table S1. The results suggest that the diffusion-limited marker $K_4Fe(CN)_6$/ $K_3Fe(CN)_6$ does not show significant change in current values for different electrode morphologies. However, on the contrary, the surface-confined marker (Fc-SH) reveals larger changes. This is due to the fast reaction kinetics of $[Fe(CN)_6]^{3-/4-}$ leading to the consumption of redox molecules in the solution via oxidation and not having sufficient time to permeate deeper into the pores. Put another way, in this case the diffusion-limited redox molecule cannot electrochemically access the entire porous surface. These results are in line with the previous

research on nanostructured electrodes confirming that the faradaic response for a surface bound marker is governed by the np-Au surface area whereas in case of diffusion limited marker, the response is determined only by the surface accessible area to the redox marker [9, 27-28 40].

3.4. Probe DNA Immobilization on Electrode Morphology Library

Informed by both our and previously reported results revealing that *surface-bound* (as opposed to *diffusion-controlled*) redox molecules are needed to fully access the np-Au surface[9, 27-28], methylene blue (MB) was selected as it specifically binds to ssDNA via ionic interactions and a□nity bindings with free guanine bases which decreases in hybridized dsDNA[33,34,41]. The next set of experiments couple MB with DNA-functionalized np-Au EML, displaying various electrode morphologies for characterizing the biosensor. The EML was produced by electrically addressing individual electrodes on the np-Au MEA with the potentiostat and cycling them over a potential range 0.3 to 1.2 V for arbitrary cycle numbers. This protocol was successful in creating an EML (Figure 2A), which was then modified with thiolated DNA probe molecules and further incubated with MB. Figure 2B illustrates the SWV signal (due to MB-ssDNA binding) obtained from the probe DNA-functionalized electrodes in PBS having different levels of coarsening. The uncoarsened np-Au electrode produced the highest MB reduction current indicating the highest DNA grafting (Figure 2B), while the peak MB current decreased with increasing coarsening. This decrease is attributed to the decreasing electrode surface area with increased coarsening (as observed in effective surface area determination Figure S2). A similar observation was made when SWV was performed in FBS instead of PBS (Figure S5).

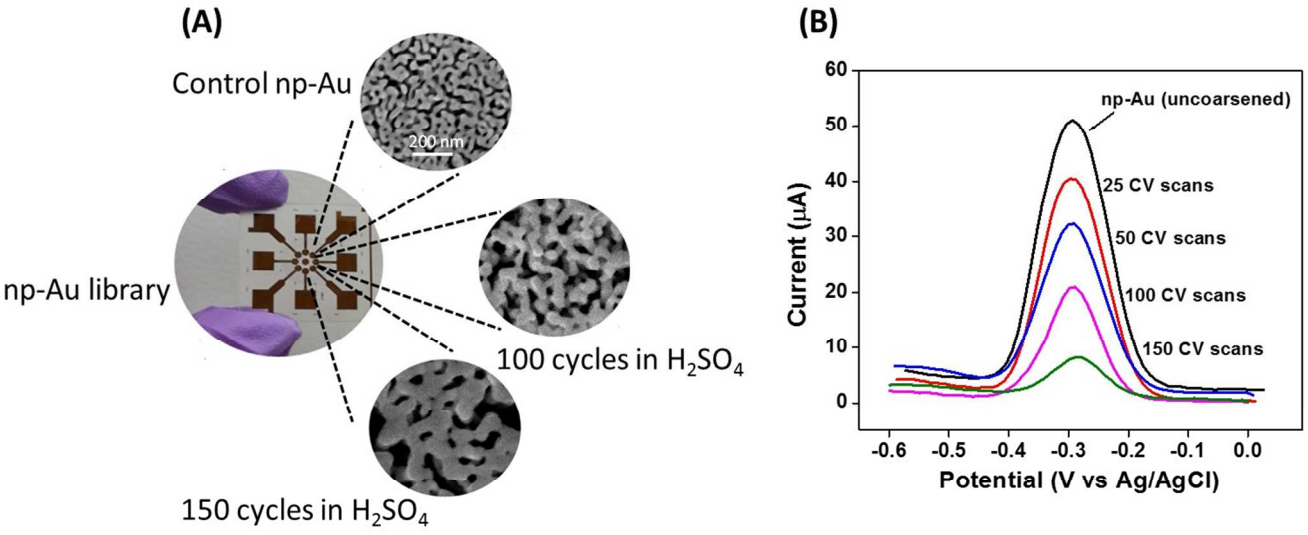

Figure 2. (A) Optical micrograph of the multiple electrode arrays and SEM images illustrating different np-Au morphologies on the electrode morphology library (EML). (B) Square wave voltammetry measurements for DNA-functionalized EML in 1X PBS.

3.5. Target DNA Detection in Phosphate Buffer Saline

Following the immobilization of probe DNA, the EML was challenged with detection of a fully-complementary target DNA (50 nM, mid-point in limit of detection based on previous studies)[23]. The change in SWV signal (i.e., % signal suppression, which dictates limit of detection) was measured via ssDNA and dsDNA interaction with MB for each np-Au electrode of different morphology (Figure 3A-C). To decouple the influence of surface area on probe DNA grafting and target hybridization on each electrode, we plotted the current obtained for probe DNA on each morphology and signal suppression obtained for each sensing electrode after target binding (Figure 3D). The peak current for probe DNA decreased for coarser morphologies due to the reduced surface area, while on the contrary the signal for target binding increased due to better accessibility of target DNA through the larger pores (Figure 3E). It is important to note that the level of coarsening inversely influences the two important sensor parameters here. These two parameters break even at around a pore radius of 30 nm (shown by shaded region), revealing a morphology range that should allow for enhanced biosensor performance in detecting target DNA in PBS. It should be noted that although the pore sizes greater than 30 nm lead to a higher signal suppression value (~70%) indicating a better limit of detection for larger pores, the early saturation of the sensor surface for larger pores (due to reduced surface area with coarsening, Figure S2) obviates this advantage.

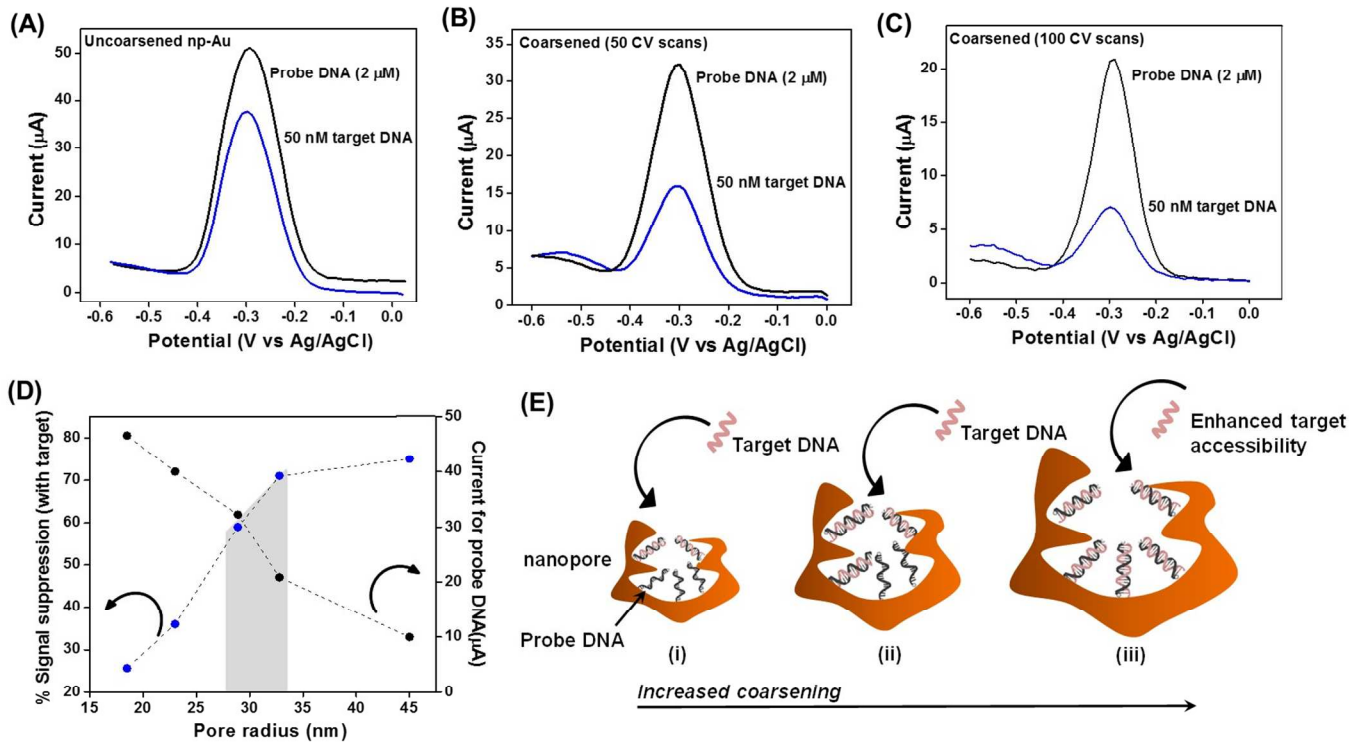

Figure 3. SWV signal of probe and target DNA in PBS for (A) uncoarsened np-Au and (B, C) gradually coarsened np-Au electrodes. (D) Probe signals at EML and the corresponding sensor responses for each electrode morphology, highlighting the break-even morphology (i.e., pore radius range) that maximizes both sensor performance parameters. Signal suppression was defined as $(I_{probe} - I_{target}/I_{probe}) \times 100$. (E) Pictorial presentation of hybridization event in uncoarsened and systemically-coarsened np-Au electrodes. The peak current signal from DNA decreased for coarser morphologies due to reducing surface area. However, accessibility of target DNA increased with bigger pores in the coarsened morphology, which results in higher signal suppression for coarsened morphologies[23].

3.6. Target DNA Detection in Fetal Bovine Serum

Biofouling of the sensing electrode surface in a complex biological environment has been a persistent challenge for electrochemical sensing devices[4]. The non-specific large biomolecules present in complex media such as proteins, lipids, polysaccharides collect on the sensor surface and hinder binding of specific target with the probe, as well as impede the charge transfer between the redox reporters and the electrode. We have previously demonstrated enhanced detection of target DNA in biofouling solutions such as bovine serum albumin and FBS using

np-Au electrodes[14]. Here, we apply the EML to elucidate the effect of np-Au morphology on the extent of biomolecule adsorption and target transport, thus sensing performance, for different electrode morphologies (Figure 4A-C). As seen in Figure 4D, while the signal for ssDNA monotonously decreased for coarser morphologies similar to the previous PBS case (Figure 3D), the signal suppression increased up to a pore radius of 30 nm but decreased sharply afterwards (Figure 4D). This non-monotonous trend in signal suppression is attributed to coarser morphologies increasing accessibility of target DNA while sieving the large proteins up to a pore size of 30 nm. After this point the pores are too large to efficiently sieve out non-specific FBS constituents that permeate the deeper surfaces and hinder target and redox transport (Figure 4E). Taken together, the optimal detection in complex biological samples appear to be achieved by np-Au with 25 nm to 30 nm average pore radii.

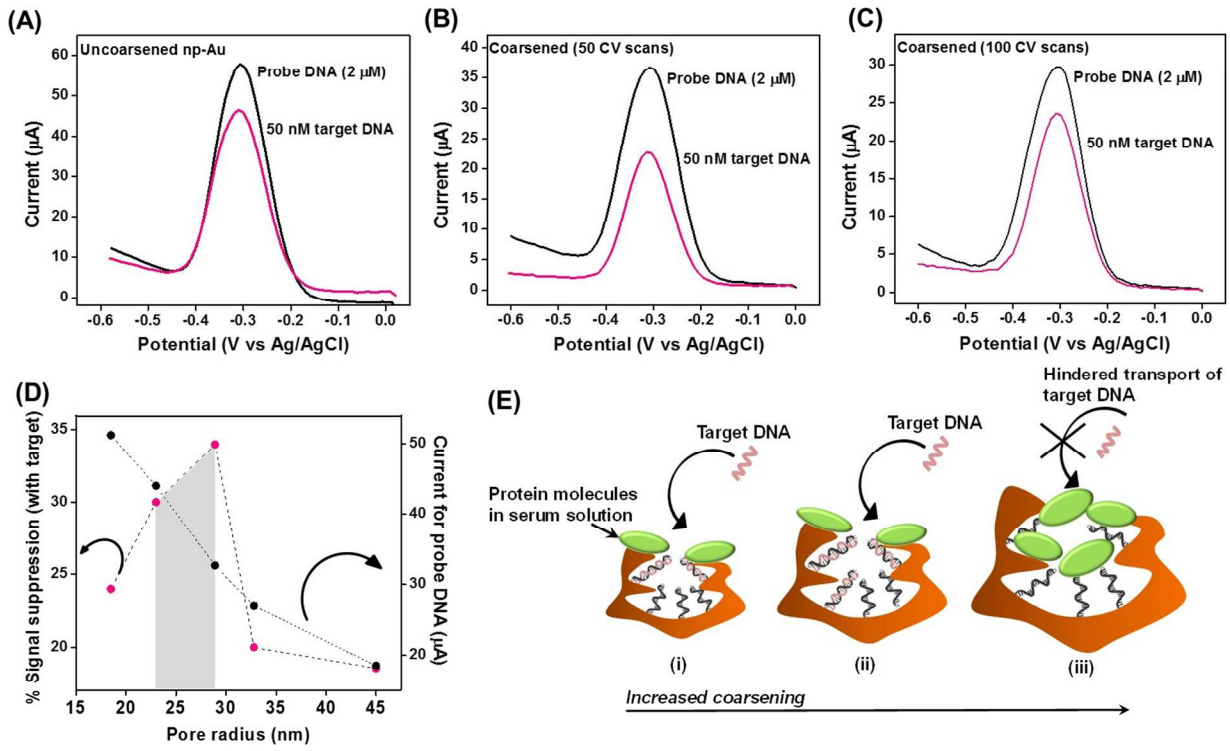

Figure 4. (A) SWV signal of probe and target DNA in FBS for (A) uncoarsened np-Au and (B, C) gradually coarsened np-Au electrodes. (D) Probe signals at different coarsened np-Au electrodes and the corresponding sensor responses from each electrode. Signal suppression was defined as $(I_{probe}-I_{target}/I_{probe}) \times 100$. (E) Small pores of uncoarsened np-Au electrodes did not permit large biofouling molecules to permeate the porous network; however, highly coarsened np-Au electrodes suffered from extensive biofouling and resulted in a decrease in the sensor performance.

4. CONCLUSIONS

We employed an electrochemical coarsening method to create an EML of np-Au for the systematic study of how electrode morphology dictates electrochemical DNA sensor performance. Specifically, for coarser morphologies, the MB peak current from immobilized probe DNA decreased due to a reduction in effective surface area, while signal suppression (measure of target DNA detection performance) increased due to better access to target DNA in PBS. For complex biological media (i.e., FBS), there was a monotonic dependence of signal suppression on pore size, where small pores exhibited biofouling resilience enhancing detection performance while larger pores became more susceptible to electrode blockage due to biofouling thereby leading to deterioration in detection performance. All taken together, the EML was able to reveal a range of average pore radii (25 nm to 30 nm) that maximizes the DNA detection performance in biofouling conditions, which is a superposition of peak current, signal suppression, and biofouling resilience as a complex function of morphology. Since the EML construction is microfabrication compatible, it is easy to scale the libraries up to a much larger set of morphologies and employ them not only for biosensing studies, but also investigating structure-property relationships in neural electrodes and battery applications.

ASSOCIATED CONTENT

Supporting Information

The Supporting Information is available free of charge on the ACS Publications website. SEM characterization of morphologies obtained in different potential ranges, Electrochemical characterization in potassium ferro-/ferri-cyanide and 6-(ferrocenyl)hexanethiol, SWV for probe DNA functionalization EML in FBS.

AUTHOR INFORMATION

Corresponding Author

*E-mail: eseker@ucdavis.edu

Notes

The authors declare no competing financial interest.

ACKNOWLEDGEMENTS

We acknowledge funding from UC Lab Fees Research Program Award (12-LR-237197), UC Davis Research Investments in the Sciences & Engineering (RISE) Award, and National Science Foundation Awards (CBET-1512745 and CBET&DMR-1454426). We also thank Jovana Veselinovic and Rijuta Ravichandran for elemental composition studies, and Prof. Joshua Hihath for discussions on DNA-surface interactions.

REFERENCES

1. Odenthal, K. J.; Gooding, J. J. An Introduction to Electrochemical DNA Biosensors. *Analyst* **2007,** *132* (7), 603-610.

2. Matharu, Z.; Bandodkar, A. J.; Gupta, V.; Malhotra, B. D. Fundamentals and Application of Ordered Molecular Assemblies to Affinity Biosensing. *Chem. Soc. Rev.* **2012,** *41* (3), 1363-1402.

3. Barfidokht, A.; Gooding, J. J. Approaches toward Allowing Electroanalytical Devices to Be Used in Biological Fluids. *Electroanalysis* **2014,** *26* (6), 1182-1196.

4. Ferguson, B. S.; Hoggarth, D. A.; Maliniak, D.; Ploense, K.; White, R. J.; Woodward, N.; Hsieh, K.; Bonham, A. J.; Eisenstein, M.; Kippin, T. E. Real-Time, Aptamer-Based Tracking of Circulating Therapeutic Agents in Living Animals. *Sci. Transl. Med.* **2013,** *5* (213), 213ra165-213ra165.

5. Patel, A. C.; Li, S.; Yuan, J.-M.; Wei, Y. In Situ Encapsulation of Horseradish Peroxidase in Electrospun Porous Silica Fibers for Potential Biosensor Applications. *Nano Lett.* **2006,** *6* (5), 1042-1046.

6. Lee, D.; Lee, J.; Kim, J.; Kim, J.; Na, H. B.; Kim, B.; Shin, C. H.; Kwak, J. H.; Dohnalkova, A.; Grate, J. W.; Hyeon, T.; Kim, H. S. Simple Fabrication of a Highly Sensitive and Fast Glucose Biosensor Using Enzymes Immobilized in Mesocellular Carbon Foam. *Adv. Mater.* **2005,** *17* (23), 2828-2833.

7. Wang, J. Nanomaterial-Based Electrochemical Biosensors. *Analyst* **2005,** *130* (4), 421-426.

8. Gurudayal; Chiam, S. Y.; Kumar, M. H.; Bassi, P. S.; Seng, H. L.; Barber, J.; Wong, L. H. Improving the Efficiency of Hematite Nanorods for Photoelectrochemical Water Splitting by Doping with Manganese. *ACS Appl. Mater. Interfaces* **2014,** *6* (8), 5852-5859.

9. Patel, J.; Radhakrishnan, L.; Zhao, B.; Uppalapati, B.; Daniels, R. C.; Ward, K. R.; Collinson, M. M. Electrochemical Properties of Nanostructured Porous Gold Electrodes in Biofouling Solutions. *Anal. Chem.* **2013,** *85* (23), 11610-11618.

10. Zhang, L.; Webster, T. J. Nanotechnology and Nanomaterials: Promises for Improved Tissue Regeneration. *Nano Today* **2009,** *4* (1), 66-80.

11. Li, Y.; Liu, Y.; Liu, J.; Liu, J.; Tang, H.; Cao, C.; Zhao, D.; Ding, Y. Molecularly Imprinted Polymer Decorated Nanoporous Gold for Highly Selective and Sensitive Electrochemical Sensors. *Sci. Rep.* **2015,** *5*, 7699.

12. Lang, X.-Y.; Fu, H.-Y.; Hou, C.; Han, G.-F.; Yang, P.; Liu, Y.-B.; Jiang, Q. Nanoporous Gold Supported Cobalt Oxide Microelectrodes as High-Performance Electrochemical Biosensors. *Nat. Commun.* **2013,** *4*, 2169.

13. Xue, Y.; Markmann, J.; Duan, H.; Weissmüller, J.; Huber, P. Switchable Imbibition in Nanoporous Gold. *Nat. Commun.* **2014,** *5*, 4237.

14. Daggumati, P.; Matharu, Z.; Wang, L.; Seker, E. Biofouling-Resilient Nanoporous Gold Electrodes for DNA Sensing. *Anal. Chem.* **2015,** *87* (17), 8618-8622.

15. Biener, J.; Wittstock, A.; Zepeda-Ruiz, L. A.; Biener, M. M.; Zielasek, V.; Kramer, D.; Viswanath, R. N.; Weissmuller, J.; Baumer, M.; Hamza, A. V. Surface-Chemistry-Driven Actuation in Nanoporous Gold. *Nat. Mater.* **2009,** *8* (1), 47-51.

16. Ding, Y.; Erlebacher, J. Nanoporous Metals with Controlled Multimodal Pore Size Distribution. *J. Am. Chem. Soc.* **2003,** *125* (26), 7772-7773.

17. Seker, E.; Gaskins, J. T.; Bart-Smith, H.; Zhu, J.; Reed, M. L.; Zangari, G.; Kelly, R.; Begley, M. R. The Effects of Post-Fabrication Annealing on the Mechanical Properties of Freestanding Nanoporous Gold Structures. *Acta Mater.* **2007,** *55* (14), 4593-4602.

18. Fischer, L. M.; Tenje, M.; Heiskanen, A. R.; Masuda, N.; Castillo, J.; Bentien, A.; Émneus, J.; Jakobsen, M. H.; Boisen, A. Gold Cleaning Methods for Electrochemical Detection Applications. *Microelectron. Eng.* **2009,** *86* (4), 1282-1285.

19. Pemberton, J. E.; Guy, A. L.; Sobocinski, R. L.; Tuschel, D. D.; Cross, N. A. Surface Enhanced Raman Scattering in Electrochemical Systems: The Complex Roles of Surface Roughness. *Appl. Surf. Sci.* **1988,** *32* (1–2), 33-56.

20. Abeera, S.; Jay, K. B.; Allan, J. A.; Alexei, V. D.; Keith, J. S. Electrochemical Annealing of Nanoporous Gold by Application of Cyclic Potential Sweeps. *Nanotechnology* **2015,** *26* (8), 085602.

21. Dursun, A.; Pugh, D. V.; Corcoran, S. G. Dealloying of Ag-Au Alloys in Halide-Containing Electrolytes: Affect on Critical Potential and Pore Size. *J. Electrochem. Soc.* **2003,** *150* (7), B355-B360.

22. Doña, J. M.; González-Velasco, J. The Dependence of the Surface Diffusion Coefficients of Gold Atoms on the Potential: Its Influence on Reconstruction of Metal Lattices. *Surf. Sci.* **1992,** *274* (2), 205-214.

23. Daggumati, P.; Matharu, Z.; Seker, E. Effect of Nanoporous Gold Thin Film Morphology on Electrochemical DNA Sensing. *Anal. Chem.* **2015,** *87* (16), 8149-8156.

24. Daggumati, P.; Kurtulus, O.; Chapman, C. A. R.; Dimlioglu, D.; Seker, E. Microfabrication of Nanoporous Gold Patterns for Cell-Material Interaction Studies. *J. Visualized Exp.* **2013,** *77*, e50678- e50678.

25. Baker, C. A.; Bulloch, R.; Roper, M. G. Comparison of Separation Performance of Laser-Ablated and Wet-Etched Microfluidic Devices. *Anal. Bioanal. Chem.* **2011,** *399* (4), 1473-1479.

26. Hu, X.; Wang, R.; Ding, Y.; Zhang, X.; Jin, W. Electrochemiluminescence of Cdte Quantum Dots as Labels at Nanoporous Gold Leaf Electrodes for Ultrasensitive DNA Analysis. *Talanta* **2010,** *80* (5), 1737-1743.

27. Scanlon, M. D.; Salaj-Kosla, U.; Belochapkine, S.; MacAodha, D.; Leech, D.; Ding, Y.; Magner, E. Characterization of Nanoporous Gold Electrodes for Bioelectrochemical Applications. *Langmuir* **2012,** *28* (4), 2251-2261.

28. Anandan, V.; Yang, X.; Kim, E.; Rao, Y. L.; Zhang, G. Role of Reaction Kinetics and Mass Transport in Glucose Sensing with Nanopillar Array Electrodes. *J. Biol. Eng.* **2007,** *1*, 5-5.

29. Creager, S. E.; Rowe, G. K., Solvent and Double-Layer Effects on Redox Reactions in Self-Assembled Monolayers of Ferrocenyl—Alkanethiolates on Gold. *J. Electroanal. Chem.* **1997,** *420* (1), 291-299.

30. Lin, X.-H.; Wu, P.; Chen, W.; Zhang, Y.-F.; Xia, X.-H. Electrochemical DNA Biosensor for the Detection of Short DNA Species of Chronic Myelogenous Leukemia by Using Methylene Blue. *Talanta* **2007,** *72* (2), 468-471.

31. Yang, W.; Ozsoz, M.; Hibbert, D. B.; Gooding, J. J. Evidence for the Direct Interaction between Methylene Blue and Guanine Bases Using DNA-Modified Carbon Paste Electrodes. *Electroanalysis* **2002,** *14* (18), 1299-1302.

32. Gu, J.; Lu, X.; Ju, H. DNA Sensor for Recognition of Native Yeast DNA Sequence with Methylene Blue as an Electrochemical Hybridization Indicator. *Electroanalysis* **2002,** *14* (13), 949.

33. Liu, S.-f.; Li, Y.-f.; Li, J.-r.; Jiang, L. Enhancement of DNA Immobilization and Hybridization on Gold Electrode Modified by Nanogold Aggregates. *Biosens.Bioelectron.* **2005,** *21* (5), 789-795.

34. Pan, D.; Zuo, X.; Wan, Y.; Wang, L.; Zhang, J.; Song, S.; Fan, C. Electrochemical Interrogation of Interactions between Surface-Confined DNA and Methylene Blue. *Sensors* **2007,** *7* (11), 2671-2680.

35. Dong, H.; Cao, X. Nanoporous Gold Thin Film: Fabrication, Structure Evolution, and Electrocatalytic Activity. *J. Phys. Chem. C* **2009,** *113* (2), 603-609.

36. Seebauer, E. G.; Allen, C. E. Estimating Surface Diffusion Coefficients. *Prog. Surf. Sci.* **1995,** *49* (3), 265-330.

37. Chen, A. Y.; Wang, J. W.; Wang, Y.; Jia, Y. Q.; Gu, J. F.; Xie, X. F.; Pan, D. Effects of Pore Size and Residual Ag on Electrocatalytic Properties of Nanoporous Gold Films Prepared by Pulse Electrochemical Dealloying. *Electrochim. Acta* **2015,** *153*, 552-558.

38. Xiao, C.; Liu, Y.-L.; Xu, J.-Q.; Lv, S.-W.; Guo, S.; Huang, W.-H. Real-Time Monitoring of H2O2 Release from Single Cells Using Nanoporous Gold Microelectrodes Decorated with Platinum Nanoparticles. *Analyst* **2015,** *140* (11), 3753-3758.

39. Tan, Y. H.; Davis, J. A.; Fujikawa, K.; Ganesh, N. V.; Demchenko, A. V.; Stine, K. J. Surface Area and Pore Size Characteristics of Nanoporous Gold Subjected to Thermal, Mechanical, or Surface Modification Studied Using Gas Adsorption Isotherms, Cyclic Voltammetry, Thermogravimetric Analysis, and Scanning Electron Microscopy. *J. Mater. Chem.* **2012,** *22* (14), 6733-6745.

40. Fan, H.; Guo, Z.; Gao, L.; Zhang, Y.; Fan, D.; Ji, G.; Du, B.; Wei, Q. Ultrasensitive Electrochemical Immunosensor for Carbohydrate Antigen 72-4 Based on Dual Signal Amplification Strategy of Nanoporous Gold and Polyaniline–Au Asymmetric Multicomponent Nanoparticles. *Biosens. Bioelectron.* **2015,** *64*, 51-56.

41. Kara, P.; Kerman, K.; Ozkan, D.; Meric, B.; Erdem, A.; Ozkan, Z.; Ozsoz, M. Electrochemical Genosensor for the Detection of Interaction between Methylene Blue and DNA. *Electrochem. Commun.* **2002,** *4* (9), 705-709.

Table of Content Graphic